Chapter 3

3.1 Introduction

In this chapter, modifications of structure, microstructure and magnetic properties of $GdMnO_3$ perovskite synthesized through sol-gel technique calcined at 1100 ºC are discussed after Fe doping. Structural and microstructural properties including J-T distortion of $GdMn_{1-x}Fe_xO_3$ ($x = 0$, 0.1 and 0.2) are discussed in section 3.2. Magnetic properties with increasing Fe concentration are analysed from M vs T, M vs H and ac susceptibility measurement in Section 3.3. Important findings of this work are summarized in Section 3.4.

3.2 Structural and Microstructural Analysis

In this section, the XRD patterns of $GdMn_{1-x}Fe_xO_3$ ($x = 0$, 0.1 and 0.2) have been analysed to verify the phase and Rietveld refinement of these data infer structural details including J-T distortion. It is further verified from Raman spectroscopy. The morphology and particle size of the samples are discussed using micrographs and particle size distribution histograms which are measured through SEM data. The oxidation state of cation and anion are discussed using XPS data.

3.2.1 X-ray diffraction: Rietveld refinement and J-T distortion

Figure 3.1 depicts the powder x-ray diffraction patterns of $GdMn_{1-x}Fe_xO_3$ ($x = 0$, 0.1 and 0.2). It is interesting to note that the sharp (*hkl*) reflections are well matched, an orthorhombic structure having space group, Pbnm (ICSD file # 250337). No trace of secondary $GdMn_2O_5$ phase has been detected in the XRD patterns, thus confirming the formation of a single phase. Previously, orthorhombic, (*Pbnm*) structure has also been observed by various authors in $GdMnO_3$ [29, 39, 80-83].

In order to comprehend the structural evolution in $GdMnO_3$ after doping Fe, x-ray diffraction patterns are fitted using the Rietveld refinement method of Fullprof program considering Pseudo-Voigt function and are shown in **figure 3.2**. The observed and refined XRD patterns are shown by black continuous lines and by red dots respectively. The difference between observed and calculated patterns (I_o- I_c) are shown at the bottom of the respective one. The tick marks above the difference patterns represent the position of the Bragg peaks. The goodness of fitting, χ^2, (given in **Table 3.1**) is very close to 1 implies that the fitting of these XRD patterns is quite good. The structural and microstructural parameters calculated from Rietveld refinement of XRD data are listed in **Table 3.1**. It is observed that while lattice parameters, a and b contract, the lattice parameter, c, shows an expansion with an increase in Fe concentration. Being an orthorhombic structure, the lattice parameters can be expressed as, $a \approx b \approx c/\sqrt{2}$. When $a< c/\sqrt{2}<b$, the structure is said to be O type orthorhombic and for O' type orthorhombic, the condition is $c/\sqrt{2}<a<b$ [84]. In the present case, a, b, and c parameters satisfy the condition for O' type orthorhombic structure irrespective of Fe concentration. While O' orthorhombic structure originates from the strong J-T distortion effect which distorts the MnO_6 octahedra, the O type structure is found to be more symmetrical in which distortion is less. Nandy et al. have also found the O' type orthorhombic structure in Na doped $GdMnO_3$ and $NdMnO_3$ [21, 84].

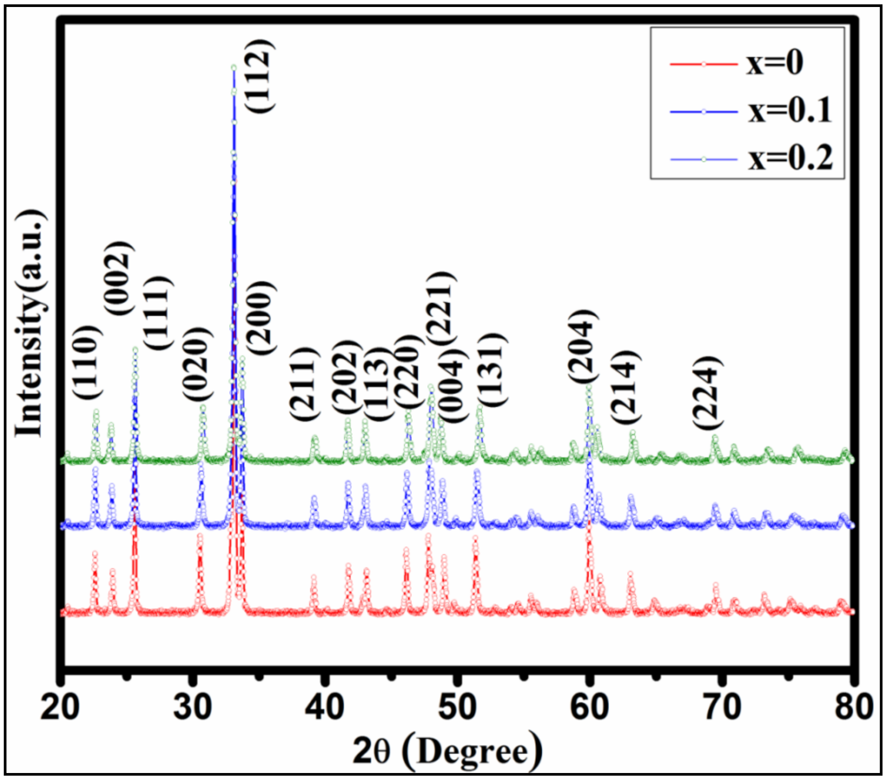

Figure 3.1 *Powder X-ray diffraction patterns of* $GdMn_{1-x}Fe_xO_3$ *(x = 0, 0.1 and 0.2).*

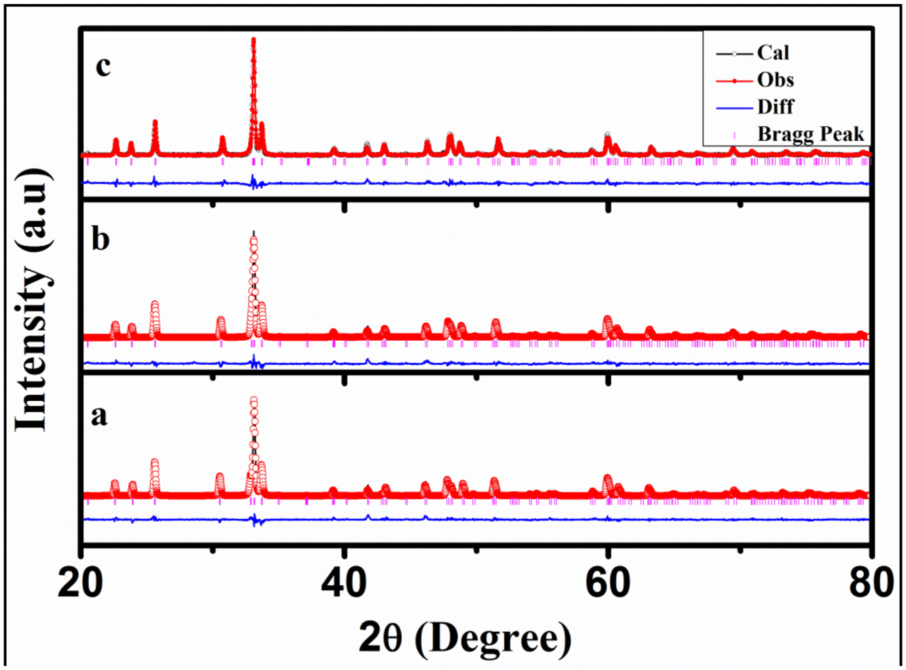

Figure 3.2 *Rietveld refinement of X-ray diffraction (XRD) patterns of* $GdMn_{1-x}Fe_xO_3$ *(a) x = 0, (b) x = 0.1 and (c) x = 0.2*

Table 3.1 Structural Parameters of $GdMn_{1-x}Fe_xO_3$ (x = 0, 0.1 and 0.2) at room temperature revealed from the Rietveld structure refinement

Parameters	x= 0	x= 0.1	x= 0.2
a (Å)	5.3154	5.3143	5.3125
b (Å)	5.8519	5.8367	5.8116
c (Å)	7.4338	7.4518	7.4690
α, β, ϒ			
V($Å^3$)	231.22	231.15	230.60
Gd (*x*, *y*, *z*)	(0.9833,0.0805,0.25)	(0.9869,0.0799,0.25)	(0.9858,0.0800,0.25)
Mn (*x*, *y*, *z*)	0.5,0,0	0.5,0,0	0.5,0,0
O1 (*x*, *y*, *z*)	(0.0965,0.4751,0.25)	(0.0633,0.5049,0.25)	(0.0826,0.4905,0.25)
O2 (*x*, *y*, *z*)	(0.7111,0.3263,0.0468)	(0.6983,0.3081, 0.0403)	(0.6903,0.3071, 0.0426)
χ^2	1.33	1.18	1.11
Mn-O1(Å)	1.93	1.93	1.92
Mn-O2 (Å)(*l*)	2.24	2.11	2.07
Mn-O2' (Å)(*s*)	1.87	1.98	2.02
Mn-O1-Mn(deg)	148	150.0	153.3
Mn-O2-Mn(deg)	147.5	147.7	148.3
$<\omega>$	32.27	31.70	29.17
$\lvert a-b \rvert$	0.5365	0.5224	0.4991
$<cos^2\theta>$	0.71	0.72	0.76

Moreover, we observe a decrease in the lattice volume from 231.22 to 230.60 Å^3 with an increase in Fe concentration. The decrease in lattice volume with Fe concentration is possibly due to the replacement of Fe either at Mn or Gd site in $GdMnO_3$. In perovskite containing Fe^{3+} and Mn^{3+}, the crystal field splitting is smaller than the Hund's energy between two electrons [85] and thus, Fe and Mn ions are in the high spin state. The ionic radius in a high spin state for both Fe and Mn in 6 coordination system are equal i.e. 0.64 Å. Thus the decrease in lattice volume could not be ascribed to the replacement of Mn^{3+} with Fe^{3+}. On the other hand, Gd has a higher ionic radius (1.107 Å), than Fe^{3+} which also eliminates the contraction in volume due to the substitution of Fe^{3+} at Gd site. If Fe^{3+} substitutes Gd, the stoichiometric of $GdMnO_3$ is lost. Therefore, the most plausible possibility could be the presence of Mn^{4+} ions which has a smaller ionic radius (0.53 Å) than Fe^{3+} and/or Mn^{3+}. The presence of Mn^{4+} ions only can reduce bond length Mn-O. The reduction in bond length reduces the volume of the MnO_6 octahedra and hence decreases the lattice volume as obtained in the present case. The presence of Mn^{4+} ion induces vacancy in oxygen sites. X-ray photoelectron spectroscopy is further carried out to examine the presence of Mn^{4+} and oxygen vacancies are discussed later.

The 3D crystal structure of $GdMn_{1-x}Fe_xO_3$ (x= 0, 0.1 and 0.2) generated from the refined structural parameters including atomic positions using Vista software is shown in **figure 3.3**. After doping 10 and 20 % of Fe^{3+}, Mn^{3+} ions are replaced by Fe^{3+} ions (brown color) shown in **figure 3.3**. The two apical positions of the MnO_6 octahedra are occupied by O1 atoms (green balls) whereas the four equatorial positions are occupied by the O2 atoms (red balls). The equatorial Mn-O2 bonds have two different bond lengths denoted as long (l) and short (s) shown in **figure 3.4**.

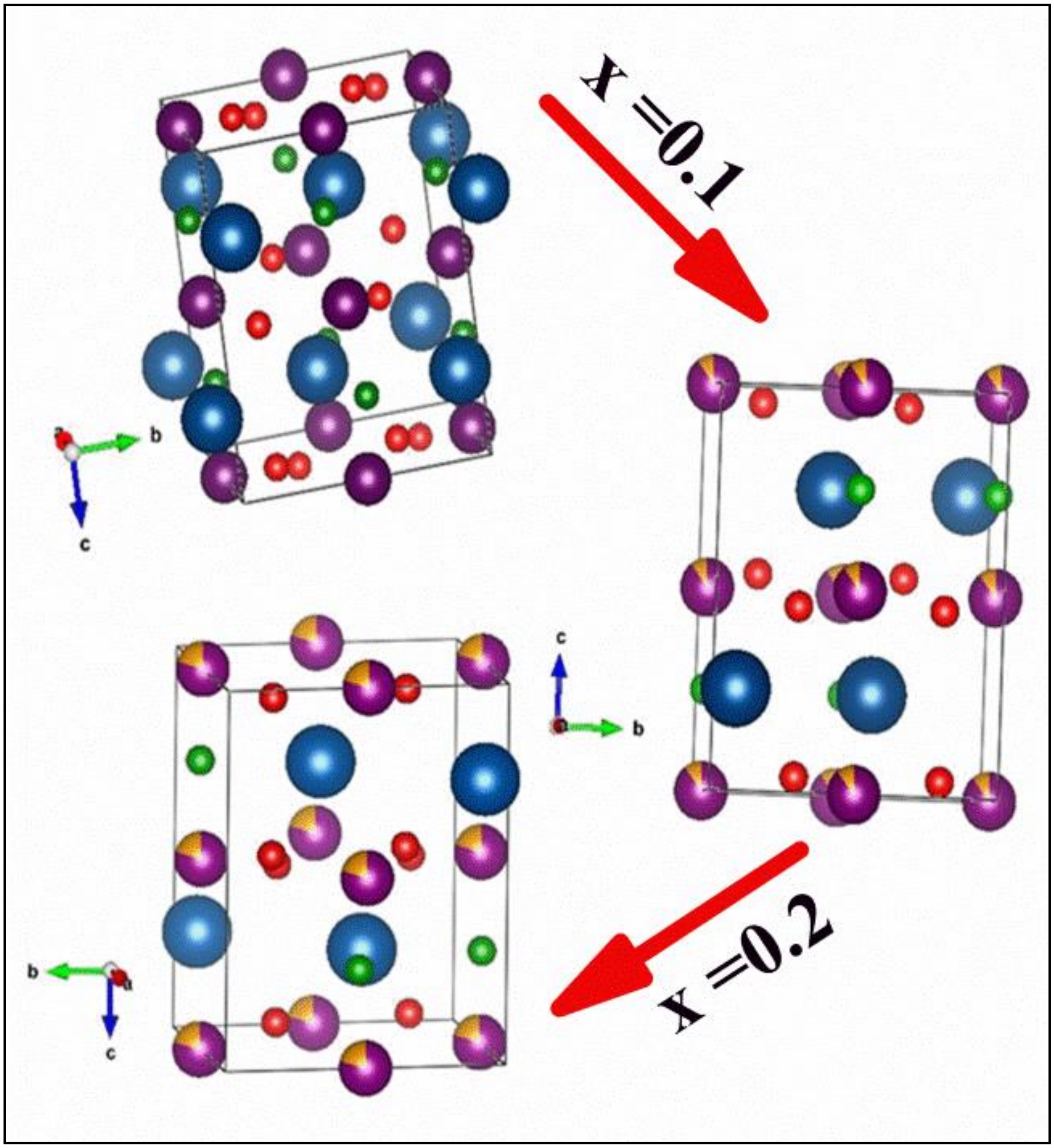

Figure 3.3 Crystal structure obtained from Rietveld refinement drawn using Vesta software.

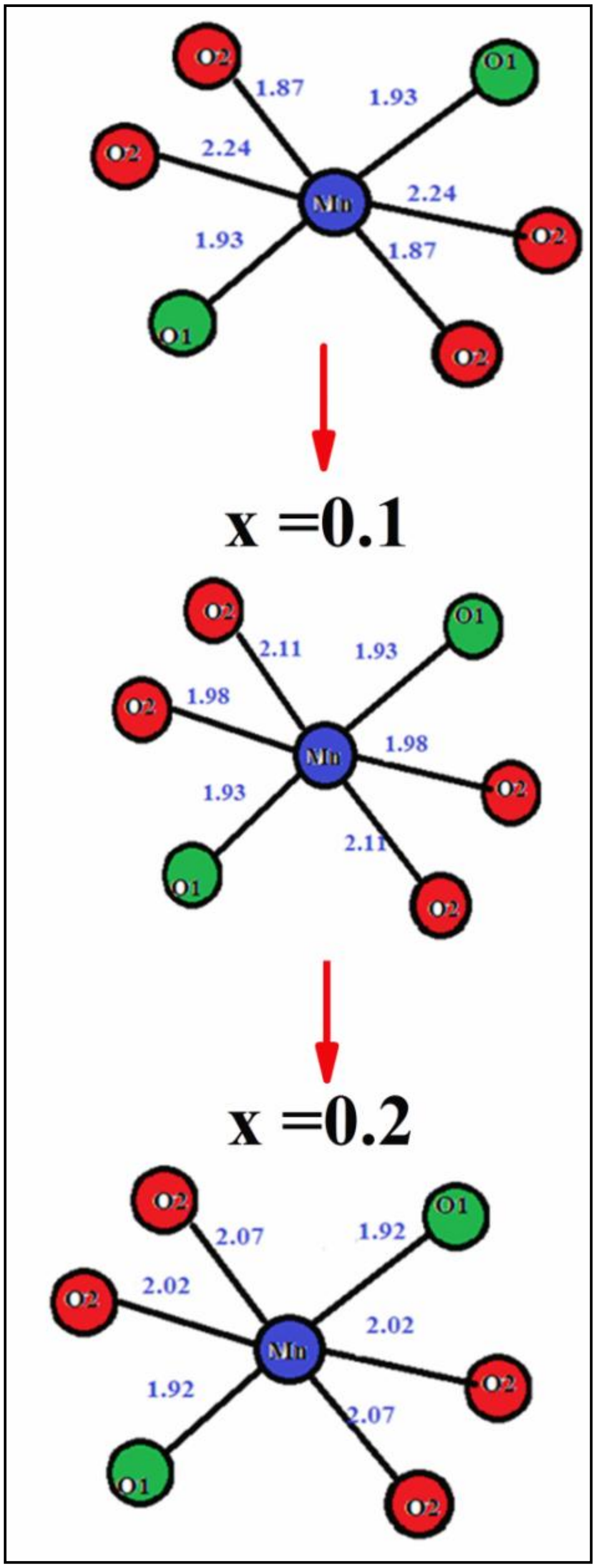

Figure 3.4 *Mn-O bond lengths of* $GdMn_{1-x}Fe_xO_3$ *(x= 0, 0.1 and 0.2) obtained from Rietveld refinement.*

In $GdMnO_3$ pervoskite structure, Mn-O bond length and Mn-O-Mn bond angle play a significant role in determining the properties of the manganite [84]. The perovskite structure of manganite is influenced by two types of distortion occurring due to, the tilting of MnO_6 octahedra or by distortions induced by the Jahn-Teller (J-T) active element like Mn^{3+} [86]. A small change in bond length Mn-O and bond angle Mn-O-Mn change the J-T distortion and the degree of tilting of octahedra. In an undistorted octahedron, one may expect the average Mn–O bond length close to the sum of ionic radii of manganese (r_{Mn}) and oxygen (r_o) i.e. 1.93 Å. In these compounds, there are one pair of Mn-O1 and two pairs of Mn-O2 bonds of different bond lengths shown in **figure 3.4**. Mn-O1, remains constant i.e., 1.93 Å (shown in Table 3.1) whereas a large deviation is observed in the bond lengths of Mn-O2 and Mn-O2'. The deviations in Mn–O bond length from1.93 Å along different directions reveal a strong J-T distortion. The J-T distortion is calculated using the following empirical relation [87],

$$\sigma_{JT}{}^{2}=1/3\Sigma_i[(Mn\text{-}O)_i-<Mn\text{-}O>] \qquad (3.1)$$

where, Mn-O and average $<Mn\text{-}O>_i$ bond lengths have been calculated from Rietveld refinement as shown in **Table 3.1**. The J-T distortion factor is found to be 0.2, 0.08 and 0.06 at x = 0, 0.1 and 0.2, respectively. One may notice that the J-T distortion factor is reduced by one order magnitude after as Fe incorporation in $GdMnO_3$. Since Fe^{3+} is not a J-T active cation like Mn^{3+}, Fe substitution thus weakens the J-T distortion releasing the orthorhombic distortion to some extent resulting in a more symmetrical structure. The results further confirm the incorporation of Fe at Mn sites. Evidence for the occurrence of J-T distortion is further quantified by considering the bond angle (θ), Mn-O-Mn. The term

$Cos^2\theta$¸ effectively measures the degree of distortion as the tolerance factor (t) is proportional to $Cos^2\theta$ [84]. The increase in average $< Cos^2\theta >$ values with Fe concentration thereby introduces a more symmetry in the structure. The deviation of average Mn-O-Mn bond angles from ideal values of 180° is measured by ω. The average $<\omega>$ in Fe doped samples is less than that of $GdMnO_3$ (**Table 3.1**). It further suggests that Fe doped $GdMnO_3$ exhibits a more symmetrical structure than that of a pristine one. The decrease in the difference of lattice parameters (|a-b|) with an increase in Fe concentration supports that the crystal system moves towards a higher structural symmetry i.e. a tetragonal unit cell [84]. The reduction in J-T distortion evidenced from Rietveld refinement is examined further through Raman measurements.

3.2.2 Raman Spectroscopy

Raman spectroscopic technique is very sensitive to the changes of symmetry and structure of the compounds. Particularly, in perovskites with *Pbnm* structure, the Raman active modes are $7A_g + 7B_{1g} + 5B_{2g} + 5B_{3g}$ [22]. These modes are active due to the deviations in the ideal perovskite structure. The Raman spectra of $GdMn_{1-x}Fe_xO_3$ (x= 0, 0.1 and 0.2) at room temperature shown in **figure 3.5** demonstrate the Raman modes at 270, 370, 487, 504 and 610 cm^{-1}. Out of these five modes, the most intense Raman mode observed at 487 cm^{-1} while attributed to the asymmetric stretching mode associated with J-T distortion produced due to Mn^{3+} ions, 610 cm^{-1} is ascribed to the symmetric stretching (SS) of basal oxygen of the octahedra [88]. The intensity of asymmetric stretching representing J-T distortion observed at 487 cm^{-1} in $GdMnO_3$ is found to decrease with an increase in Fe concentration confirming the reduction in J-T distortion evidenced from Rietveld refinement [88]. The other two vibrational modes at 370 and 505 cm^{-1} are assigned to tilting and bending of MnO_6 octahedra while the low intensity Raman mode at ~ 270 cm^{-1} is due to A_g-in plane rotation of MnO_6 octahedra [22, 88]. Although the frequency of the Raman band due to octahedral tilting although does not change, the intensity of the band is found to reduce with increase in Fe concentration (**figure 3.5**). In order to determine the valency of Mn, X-ray photoelectron spectroscopy has been employed.

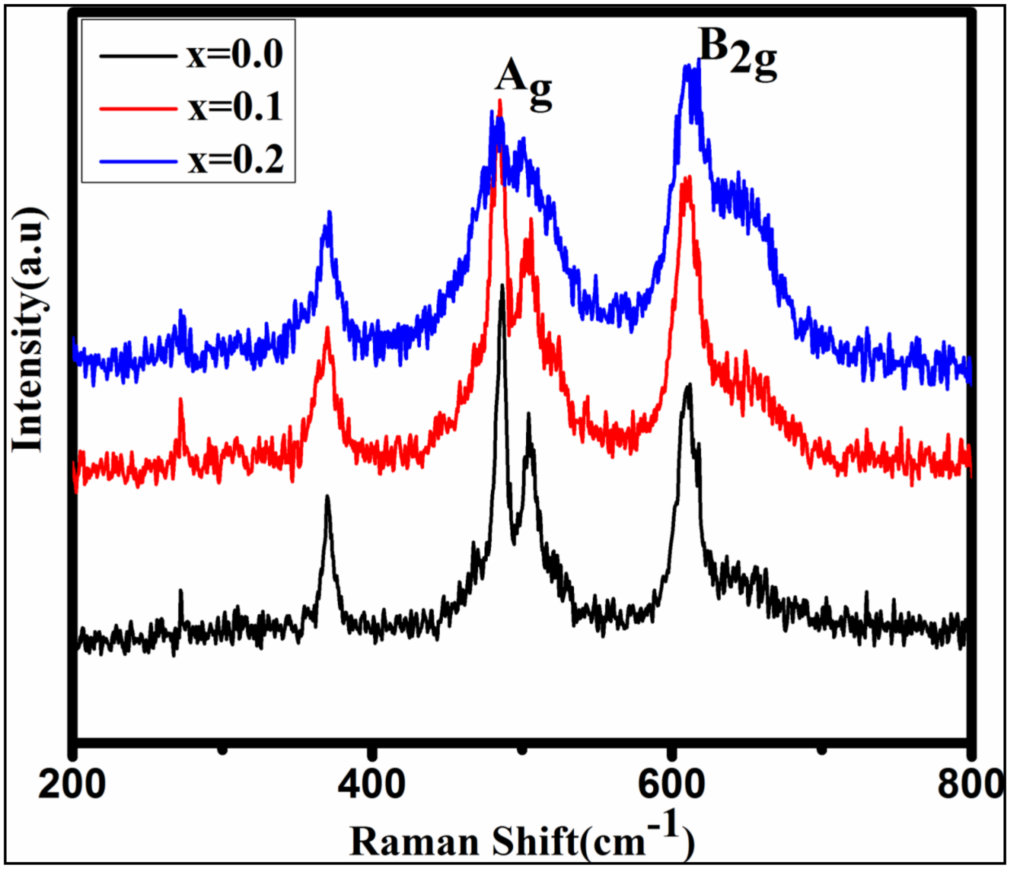

***Figure* 3.5** *Raman spectra of $GdMn_{1-x}Fe_xO_3$ (x= 0, 0.1 and 0.2).*

3.2.3 X-ray Photoelectron Spectroscopy

X-ray photoelectron spectra of $GdMn_{1-x}Fe_xO_3$ (x= 0, 0.1 and 0.2) collected using Al K_α radiation are depicted in **figure 3.6 (a)**. The core level binding energies are aligned with the carbon binding energy of 284.6 eV. The Manganese $2p_{3/2}$ core level spectra are asymmetric in nature showing maximum binding energy peak at 641.6 eV (**figure 3.6 (a)**). The asymmetric peak of Mn is fitted with two Gaussian peaks using XPS peak 4.1 software with Shirley background. The two components observed at ~641.6 and ~643.1 eV corresponds to Mn^{3+} and Mn^{4+}, respectively. The evidence of Mn^{4+} endorses the decrease in lattice volume observed from Rietveld refinement. The increase in the ratio of Mn^{4+}/Mn^{3+} from 0.35 to 0.70 with increase in Fe concentration thus confirms the reduction in J-T distortion. The 1s core level spectra of oxygen shown in **figure 3.6 (b)** is asymmetric around the binding energy, 530 eV. Therefore, spectra are fitted with two Gaussian peaks, denoted as O_a and O_b, using the aforementioned software with Shirley background. While O_a peak at 530 eV is ascribed to the lattice oxygen atoms, O_b peak at 532 eV is due to the oxygen vacancies [87]. We observe that the area ratio of O_b to O_a decreases from 1.95 to 0.63 with an increase in Fe doping indicating an increase in the concentration of oxygen vacancies. An increase in Mn^{4+} concentration thus well corroborates with decrease in oxygen vacancies induced due to the incorporation of Fe in $GdMnO_3$.

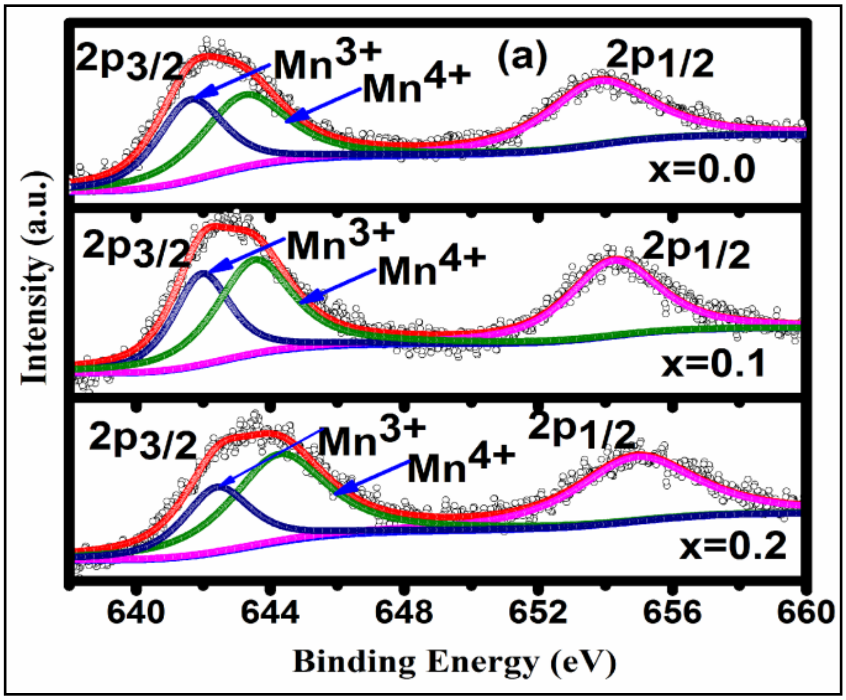

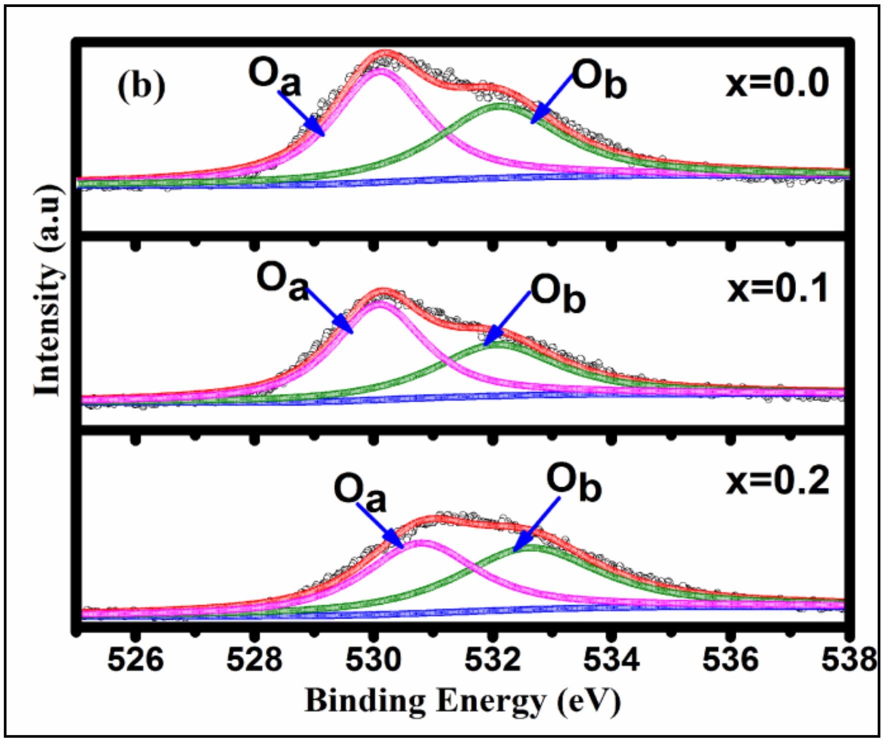

Figure 3.6 ***(a)*** *X-ray photoelectron spectroscopy for Mn 2p and* ***(b)*** *O1s of* $GdMn_{1-x}Fe_xO_3$ *(x= 0, 0.1 and 0.2).*

3.2.4 Scanning Electron Microscopy

The field emission scanning electron (FESEM) micrographs of $GdMn_{1x}Fe_xO_3$ (x=0, 0.1 and 0.2) are shown the agglomeration of the particles. The particle size distribution calculated from the micrographs is fitted with Lorentzian and log-normal distribution function after fixing the background shown in **figure 3.7(b)**. The majority of the agglomerated particles are found to be in the range of 300, 200 and 300 nm for x = 0, 0.1 and 0.2, respectively.

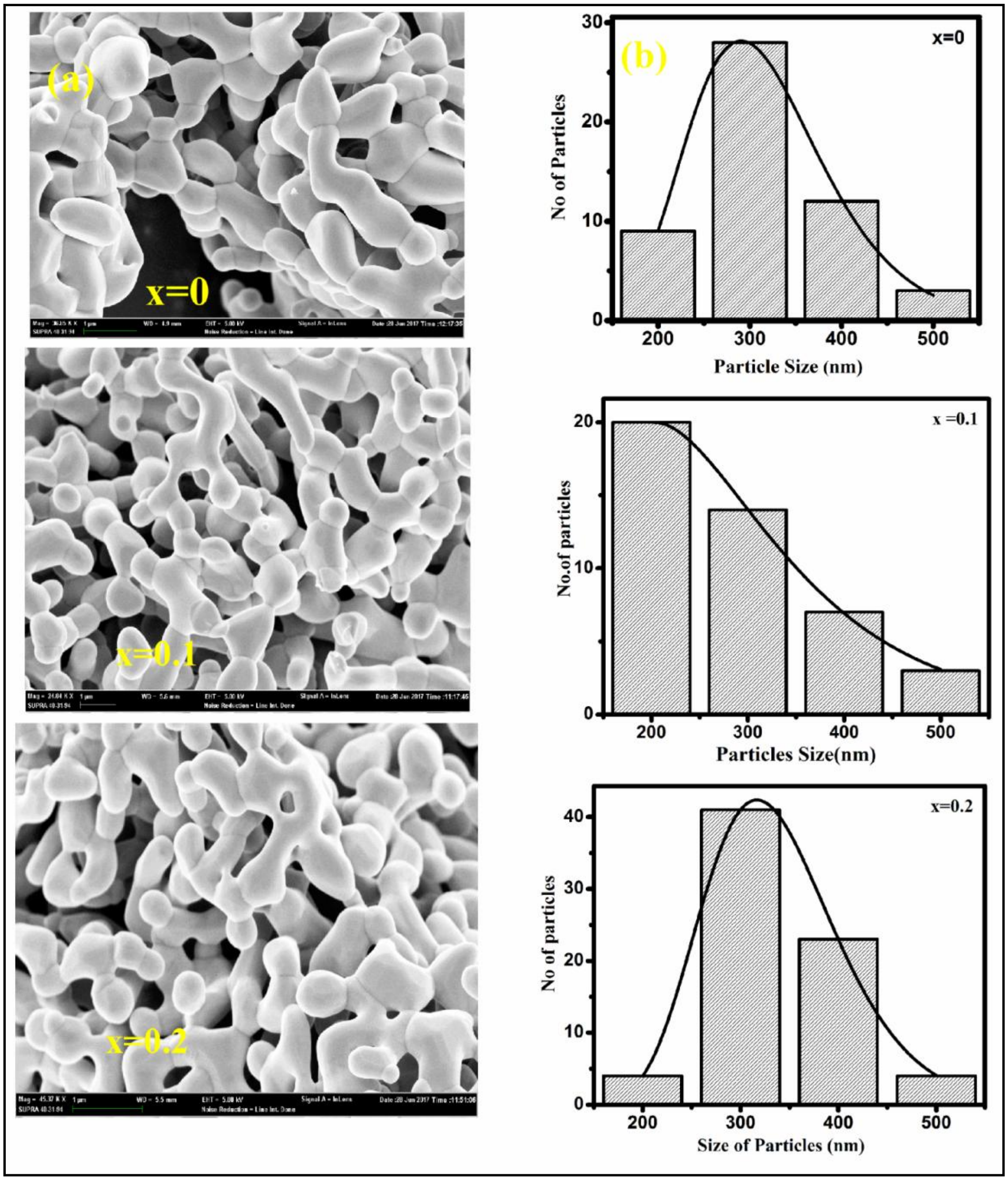

Figure 3.7 (a) *Field emission scanning electron micrographs of* $GdMn_{1-x}Fe_xO_3$ *(x= 0, 0.1 and 0.2),* ***(b)*** *shows the corresponding particle size distribution histogram.*

3.3 Magnetic Properties

To study the magnetic properties after Fe doping upto 20 at%, the temperature dependent magnetization, magnetic field dependent magnetization and temperature dependent ac susceptibility are carried out and are discussed in 3.3.1, 3.3.2 and 3.3.3, respectively.

3.3.1 Temperature dependent magnetization

The temperature dependent magnetization of $GdMn_{1-x}Fe_xO_3$ (x= 0, 0.1 and 0.2) in zero-field- cooled (ZFC) and field-cooled (FC) conditions at 0.05 and 10 kOe external magnetic field is shown in **figure 3.8**. In ZFC mode, the sample is cooled to 2 K in zero fields and in presence of an external magnetic field, magnetization is recorded as a function of temperature. However, in FC mode, the sample is cooled to 2 K in the presence of magnetic field and the magnetization is recorded with increasing temperature in the presence of external magnetic field. With decreasing temperature from 300 K, a clear bifurcation of FC and ZFC magnetization curves has been observed at a temperature which is known to be T_N. At 10 kOe, bifurcation observed in FC and ZFC magnetization disappears showing no thermo magnetic irreversibility (**figure 3.8(b))**. This is appropriate to the fact that at high magnetic field, all moments can align themselves along the field direction. To deduce the magnetic anomalies in $GdMn_{1-x}Fe_xO_3$, we have shown $1/\chi$ vs T measured at 0.05 kOe in **figure 3.9**.

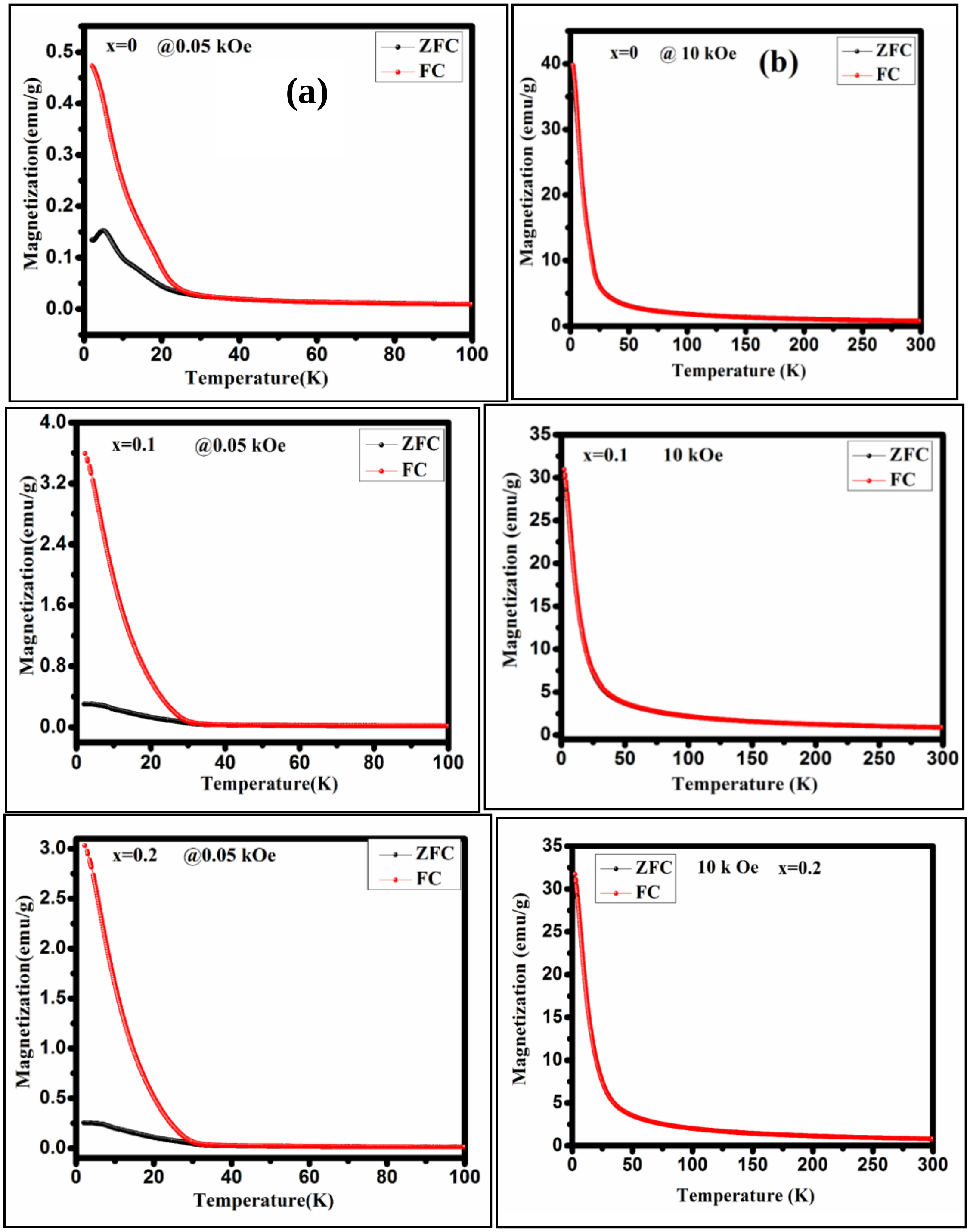

Figure 3.8 (a) *Temperature dependent magnetization under zero field cooling (ZFC) and field cooling (FC) measured at 0.050 kOe for* $GdMn_{1-x}Fe_xO_3$ *(x= 0, 0.1 and 0.2)* ***(b)*** *Temperature dependent magnetization under zero field cooling (ZFC) and field cooling (FC) measured at 10 kOe for* $GdMn_{1-x}Fe_xO_3$ *(x= 0, 0.1 and 0.2).*

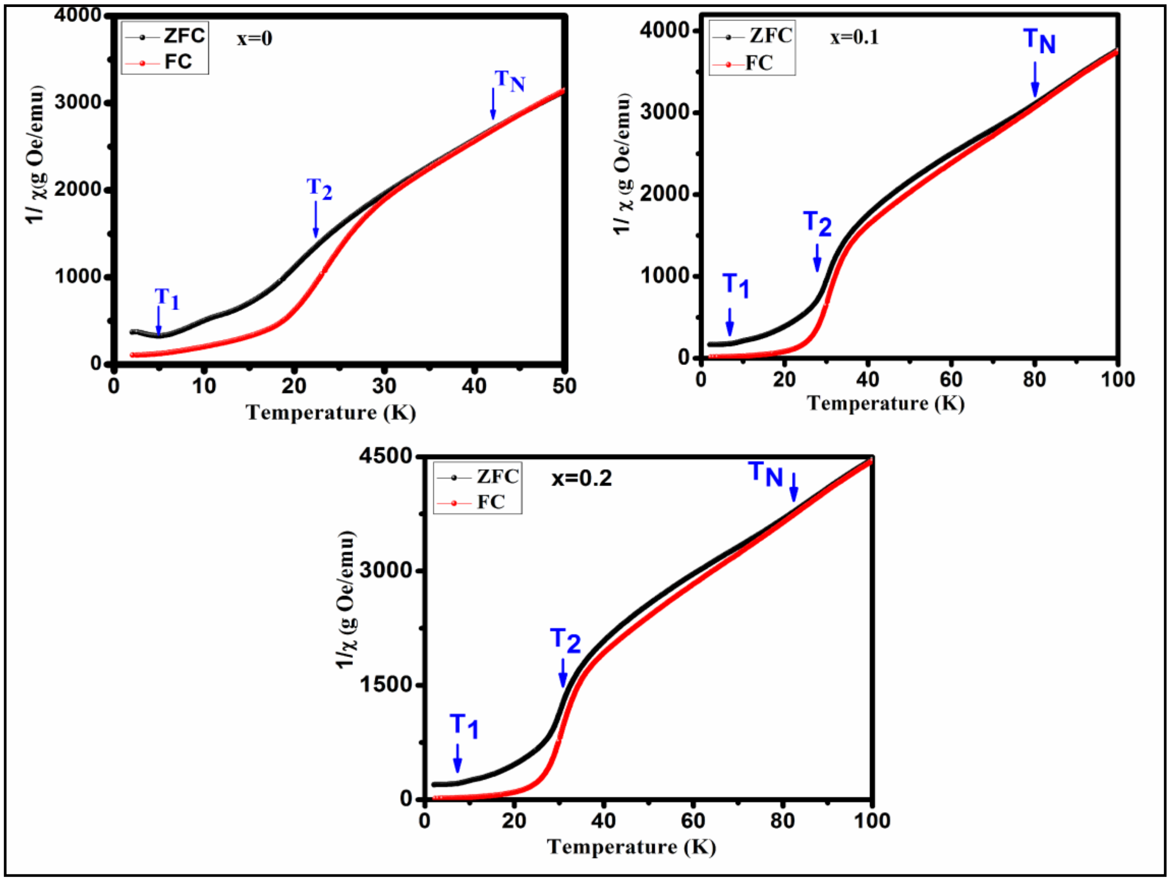

Figure 3.9 *The inverse susceptibility,* ***1/χ*** *plots of ZFC and FC in the presence of 0.050 kOe of the* $GdMn_{1-x}Fe_xO_3$ *(x= 0, 0.1 and 0.2).*

With decreasing temperature from 300 K, at around ~ 42 K, magnetization suddenly increases showing a peak at ~ 5 K in $GdMnO_3$. With increasing Fe concentration, peak position shifts to ~ 7 K for x= 0.1 and 0.2. Besides the peak at ~5 K, the slope of the curve changes at ~11 K in $GdMnO_3$. The slope at ~11 K is also shifted to ~28 K for x=0.1 and 31 K for x=0.2 (**figure 3.9**). T_N is found to be ~42, ~80 and ~84 K for x= 0, 0.1 and 0.2, respectively. T_N observed at 42 K in $GdMnO_3$ represents the transition from paramagnetic to incommensurate antiferromagnetic phase, the anomalies at ~11 and ~5 K denote the ordering of Mn^{3+} and Gd^{3+} spins, respectively. T_N in the range of 42-45 K has been reported in $GdMnO_3$ compounds by various authors [22] [21]. The observed T_N is well matched with the reported values. The polarization of Gd^{3+} spins by the canting Mn^{3+} spins results in weak ferromagnetism as observed by us below ~5 K (T_1) and corroborates with other reports [22],[21] [39],[89]]. The intermediate anomaly (T_2) observed here at ~11 K has been reported at 14 K by Fereira et al. [89]. By incorporating Fe in $GdMnO_3$ compound, we observe an increase in T_N from ~42 to ~84 K. On the contrary, T_N has been shown to decrease from ~85 K to ~36 K with an increase in Fe doping from x=0 to 0.3 in $NdMn_{1-x}Fe_xO_3$ [90]. Also in $TbMn_{1-x}FexO_3$, T_N decreases from ~ 42 K to 39 K with an increase in x from 0 to 0.02. [91]. Similar to our results, Hong et al. have also found an increase in T_N from 39 K to 680 K with increasing x from 0 to 1.0 in $DyMn_{1-x}Fe_xO_3$ [92]. The intermediate anomaly (T_2) obtained at ~11 K at x=0 shifts to ~28 and ~31K and anomaly at ~5 K (T_1) shifts to 7 K at x=0.1 and 0.2, respectively. It is expected that Fe doping can affect the magnetic exchange interaction as e_g orbital of Fe^{3+} ion is half filled and one of the states of e_g orbital of Mn^{3+} ion is unoccupied. In such cases, an occupied electronic state enhances the AFM exchange interaction like Fe incorporation does in $GdMnO_3$. In addition, increasing bond angle, Mn/Fe–O–Mn/Fe within ab-plane obtained from Rietveld refinement corroborates with the enhancement of AFM interaction and hence increases transition temperatures. Further, the variation of inverse susceptibility ($1/\chi$) with temperature in the paramagnetic region is fitted with Curie-Weiss law i.e. $1/\chi = (T-\Theta)/C$, where C is Curie constant and Θ is Curie-Weiss temperature **(figure 3.10)** [37]. The negative value of Θ varies between ~50 to ~78 K for x=0-0.2 is attributed to antiferromagnetic transition. The effective magnetic moment (μ_{eff}) calculated from Curie constant are 7.50, 9.47 and 8.63 μ_B and theoretically using the formula $\mu_{effec} = [(\mu_{Gd})^2+(1-$

$x)(\mu_{Mn})^2+x(\mu_{Fe})^2]^{1/2}$ are 7.36, 9.0 and 8.2 μ_B for x=0,0.1 and 0.2 , respectively. Both theoretical and experimental moments do not show a significant difference.

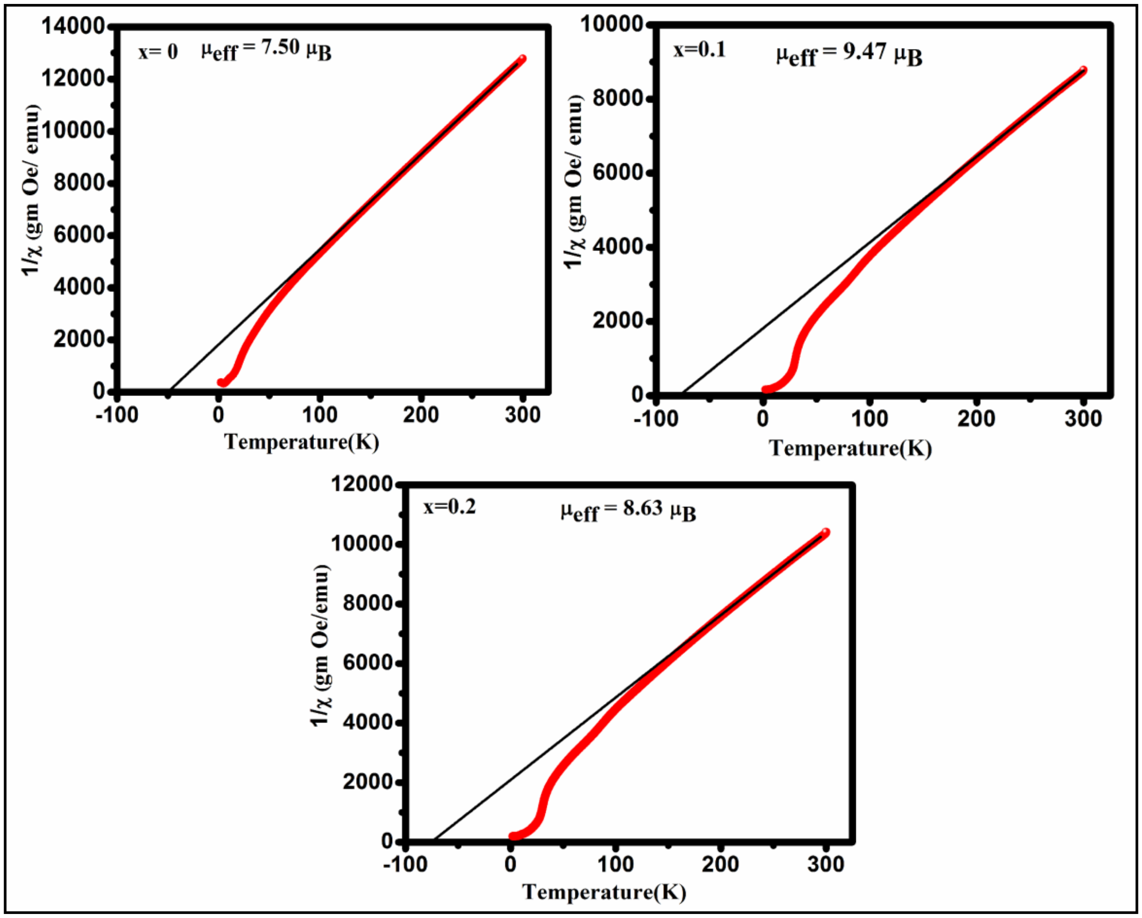

Figure 3.10 *Fitting of 1/χ vs T with Curie- Weiss law of the* $GdMn_{1-x}Fe_xO_3$ *(x= 0, 0.1 and 0.2).*

3.3.2 Field dependent magnetization

The magnetization (M) is measured with a varying external field (H) at 40, 20 and 4 K shown in **figure 3.11**. The M-H curves of $Gd_{1-x}Fe_xMnO_3$ (x= 0, 0.1, 0.2) at 40 K shows a linear increase in magnetization with increasing applied field indicating the paramagnetic nature of the particles.

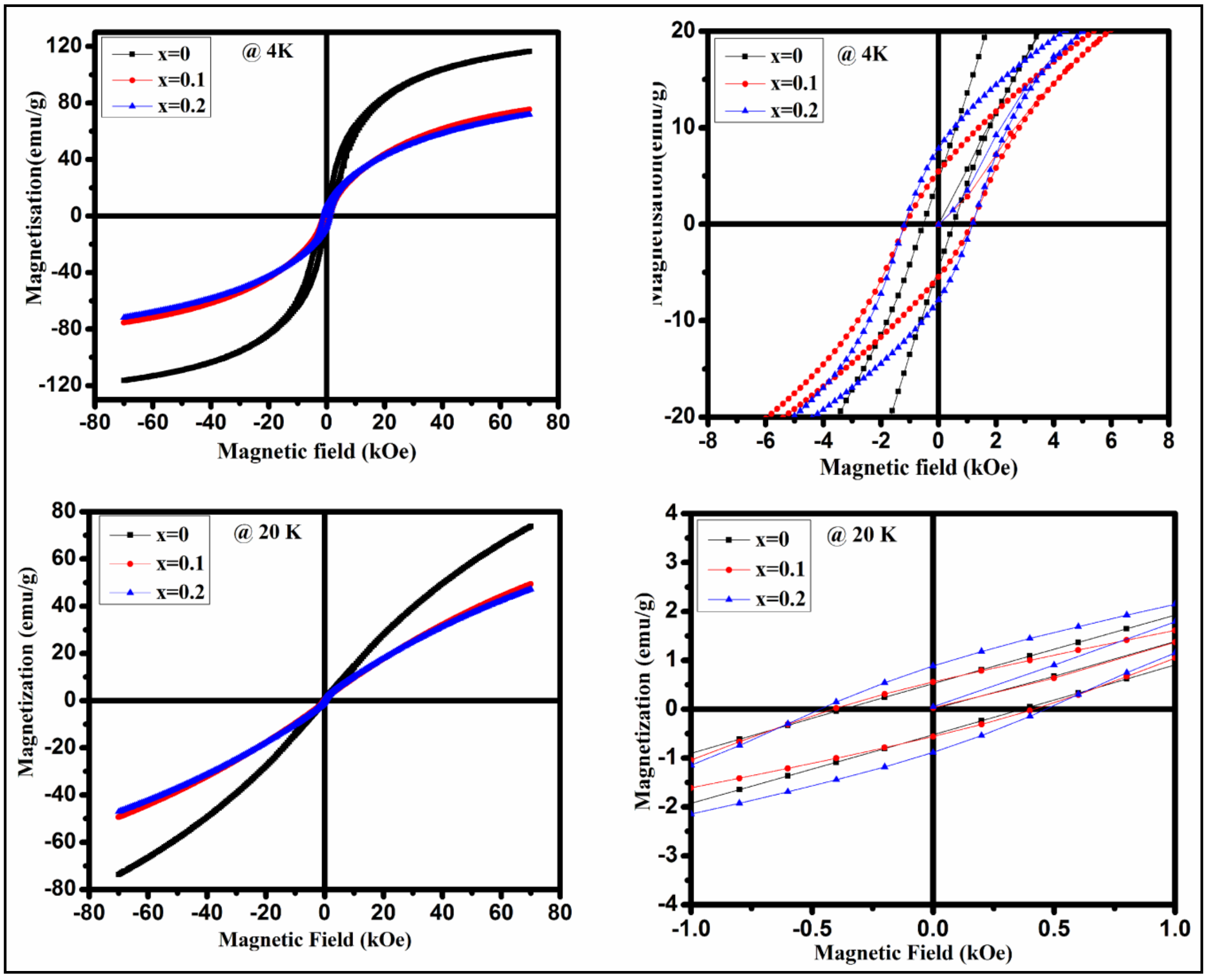

***Figure 3.11** Magnetic field-dependent magnetization at 20 and 4 K of GdMn$_{1-x}$Fe$_x$O$_3$ (x= 0, 0.1 and 0.2) with zoomed view.*

With decreasing temperature to 20 K, in addition to the linear increase in magnetization at high field, we observe a slim loop which is not saturated up to 70 kOe. The slim loop appears due to canted spins of Mn. The area under the loop increases with decreasing the temperature to 4 K. The initial magnetization curve falls out from the hysteresis loop (**figure 3.11**) may be due to uncompensated spins at the surface of the particles. Similar behavior has been reported by Ivetic et al. in Co$_3$O$_4$/SiO$_2$ nanocomposite [93]. The maximum magnetization (M$_{max}$), coercivity (H$_c$) and remanence (M$_r$) measured at 70 kOe are estimated from hysteresis loops measured at 4 and 20 K are tabulated in **Table 3.2**.

Table 3.2 Maximium magnetization (M_{max}), remanance (M_r) and coercivity (H_c) for $GdMn_{1-x}Fe_xO_3$ (x = 0, 0.1 and 0.2) at 4 K and 20 K.

Temperature	M_{max}@7 kOe (μ_B)			H_C (kOe)			M_r (μ_B)		
	x = 0	x = 0.1	x = 0.2	x = 0	x = 0.1	x = 0.2	x = 0	x = 0.1	x = 0.2
4 K	5.45	3.5	3.4	0.532	1.154	1.196	0.21	0.25	0.36
20K	3.5	2.3	2.2	0.361	0.420	0.500	0.025	0.027	0.04

While M_{max} decreases with an increase in Fe concentration, H_c and M_r are enhanced noticeably. It is quite surprising that although Fe^{3+} has a higher magnetic moment than Mn^{3+}, we observe a decrease in the magnetic moment with an increase in Fe concentration. One expects that when Fe is substituted in $GdMnO_3$, Mn ions may partially substitute the Fe ions. As a result, three combinations of bonds such as Mn-O-Mn, Mn-O-Fe, and Fe-O-Fe could coexist. However, the number of Fe-O-Fe bonds are small due to the doping amount of ~10 to 20%. Mn-O-Mn and Mn-O-Fe bonds are dominant in the mechanism of magnetic properties. It has been observed from XRD and XPS analysis that with an increase in Fe^{3+} concentration, more and more Mn^{3+} converts into Mn^{4+} ions. As Mn^{4+} is having a less moment than that of Fe^{3+} and/or Mn^{3+}, with an increase in Fe^{3+} concentration, magnetic moment thus decreases. The twice the value of H_c in x= 0.1 and x= 0.2 is explained on the basis of the bond angle which increases with an increase in Fe concentration. The enhancement in bond angle from 148 ° to 153 ° resulting in a more strong antiferromagnetic ordering which needs a higher field to demagnetize the sample. As a consequence, we observe a high coercivity with an increase in Fe concentration.

3.3.3 Temperature dependent ac susceptibility

For x = 0, besides T_1 at ~ 5 K, another magnetic anomaly appears at ~ 3 K (**figure 3.12**). With an increase in Fe concentration, the peak observed at ~ 4 K is broadened. The magnetic anomaly at the same temperature is also evidenced from the M vs T curve measured under zero field cooling. To examine the spin dynamics in these nanoparticles, real ac susceptibility at 31, 101, 299 and 501 Hz in the presence of ac field of 3 Oe have been carried out and are shown in **figure 3.12**. The maximum in AC susceptibility is recognized through the freezing temperature (T_f) i.e. the temperature at which the relaxation time, 'τ' and time scale of the experiment is the same. τ is the reverse of the measuring frequency, $\tau = 1/ f_{ac}$ [94]. With increasing frequency, T_f increases which are known to be a common characteristic feature of spin glass, cluster glass and superparamagnetic. The vital information on the relaxation dynamics can be obtained from the dependence of T_f on the measurement time τ and temperature, T. The nature of this peak (T_f) at low temperature are analyzed by different models verify the spin glass, cluster glass or superparamagnetic nature of these particles. The shift in T_f relative to different frequencies is quantitatively measured using the following formula,

$$\phi = \Delta T_f/(T_f\Delta(\log\omega)) \qquad (3.2)$$

where, Δ is the difference in related parameters [95]. Using equation (3.2), the value of ϕ are found to be 0.02, 0.01 and 0.01 for x= 0, 0.1 and 0.2. The obtained ϕ values show one order of magnitude less than the ϕ (0.1-0.3) corresponding to the non-interacting superparamagnetic particles. Tadic et al. have also found non-interacting superparamagnetic behavior in iron oxide nanoparticles in a silica matrix [94]. The estimated ϕ values lie within the reported values of ϕ for spin glass (0.005-0.06). Further, the behavior of non-interacting superparamagnetic particles are eliminated after fitting of χ' data using Neel-Arrhenius equation,

$$\tau = \tau_0 \exp\left(\frac{\mathrm{Ea}}{\mathrm{K_B T}}\right) \tag{3.3}$$

where, E_a is the anisotropy energy, k_B is Boltzmann constant and τ_0 is the time scale corresponding to that frequency (**figure 3.13)**. We have found an unphysical value of τ_0 after fitting our data (**Table 3.3**). The interacting behavior of these spins has been found out using the Vogel- Fulcher, as well as Power law, is shown as equation 3.4 and 3.5. Tadic et al. have also found out the inter-particle interaction by using Vogel- Fulcher law in case of superparamagnetic iron oxide nanoclusters [96].

Vogel–Fulcher equation $$\tau = \tau_0 \exp\left(\frac{-\mathrm{Ea}}{\mathrm{K_B}(\mathrm{T_f} - To)}\right) \tag{3.4}$$

where, T_f is the Vogel- Fulcher temperature. It is often related to the strength of τ_0 values are found to be 10^{-12}, 10^{-13} and 10^{-13} for x= 0, 0.1 and 0.2, respectively. All value of τ_0 satisfies the relaxation time (10^{-11}-10^{-13}) of atomic spin.

Power law $$\tau = \tau_0\left(\frac{\mathrm{T_f}}{\mathrm{T_g}} - 1\right)^{-zv} \tag{3.5}$$

where, z is the dynamic scaling exponent and υ is the critical exponent related to the correlation length, ξ as $\tau \alpha \xi^z$ [97]. T_g is the spin-glass transform temperature in the limit of zero frequency. The fitted data are shown in **figure 3.14** depict the τ_0 values as 10^{-9}, 10^{-12} and 10^{-11} for x=0, 0.1 and 0.2, respectively. At x= 0, τ_0 shows the flip time of cluster glass (10^{-9}-10^{-6}) [97]. Combining both the relations, we confirm that $GdMn_{1-x}Fe_xO_3$ (x= 0, 0.1

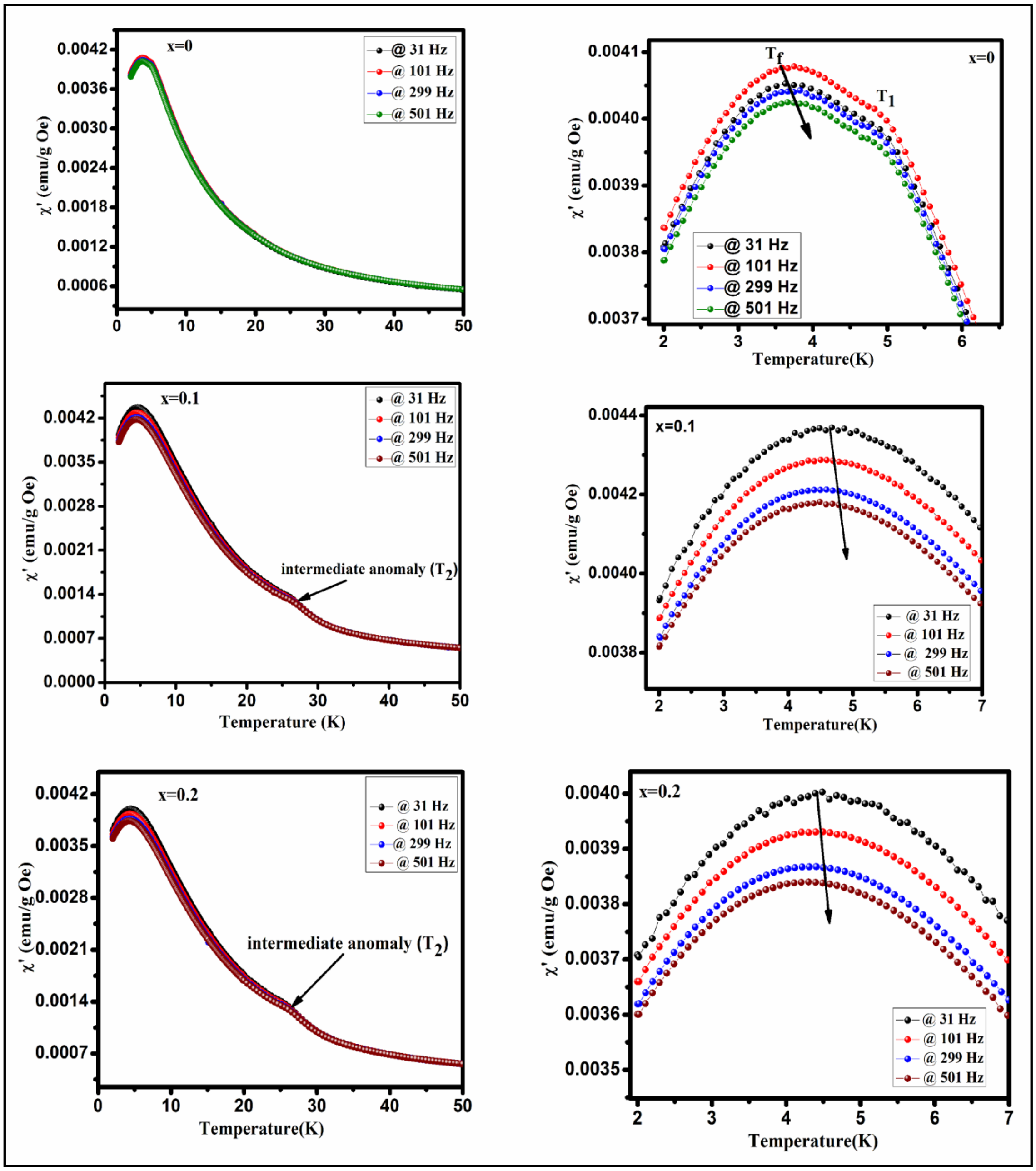

Figure 3.12 *Temperature dependence of the real part of ac susceptibility at various frequencies at the 3Oe ac field (a) x= 0 (b) x= 0.1 and (c) x= 0.2. The right panel of the respective figure shows the expanded view of the peak shift with increasing frequency.*

and 0.2) nanoparticles show a spin glass and/or cluster glass behavior. Similar spin glass behavior in K- doped $NdMnO_3$ perovskite has been reported by Nandy et al. [98]. The presence of Mn^{4+} in $GdMnO_3$ could have possible interactions with Mn^{3+} like Mn^{3+}-O2--

Mn^{3+}, Mn^{4+}- O2- Mn^{4+} and Mn^{4+}- O2-$Mn^{3+.}$ These interactions compete with each other and could show the spin glass behavior in the present case.

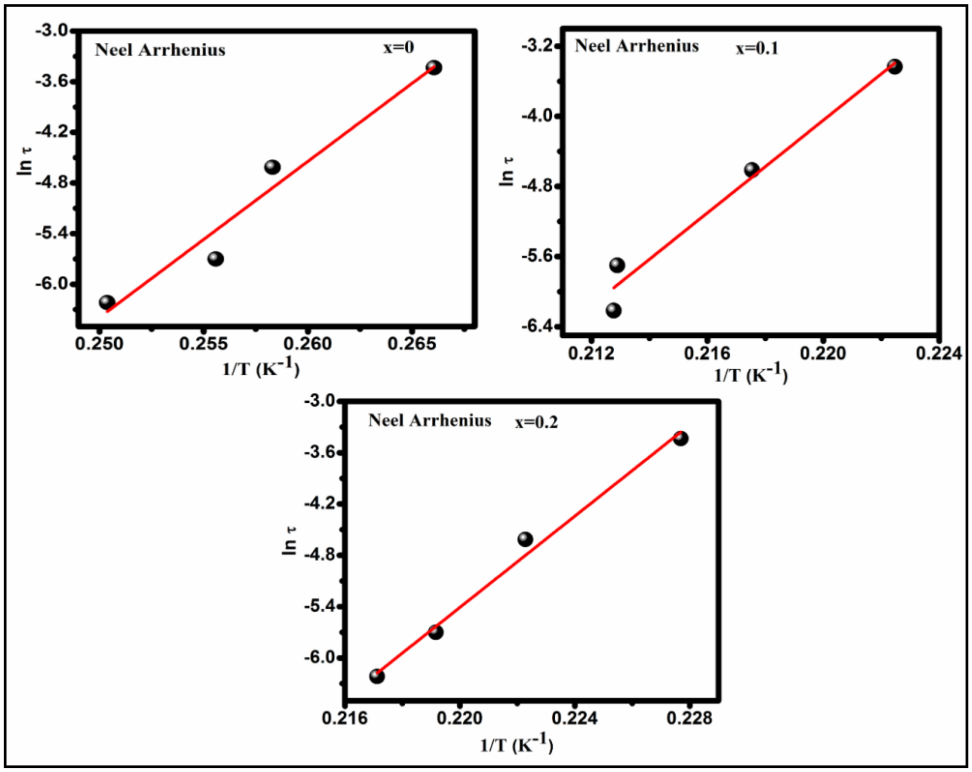

Figure 3.13 *Variation of relaxation time (τ) with T plotted with the Neel–Arrhenius fitting equation for* $GdMn_{1-x}Fe_xO_3$ *(x= 0, 0.1 and 0.2). The solid line represents the fitting.*

Table 3.3 Parameters deduced from fitting of ac susceptibility with different empirical relations such as Neel–Arrhenius, Vogel–Fulcher and Power law.

Sample	**Neel Arrhenius**	**Vogel-Fulcher**		**Power Law**		
	τ_o (sec)	***T_o***	***τ_o (sec)***	***T_g (K)***	***zU***	***τ_o (sec)***
x = 0	1.37×10^{-27}	1.9	1.56×10^{-12}	2.1	8.5	3.2×10^{-9}
x = 0.1	9.9×10^{-28}	2.6	1.15×10^{-13}	2.5	9.3	3.78×10^{-12}
x = 0.2	1.48×10^{-28}	2.8	1.80×10^{-13}	2.6	9.7	1.53×10^{-11}

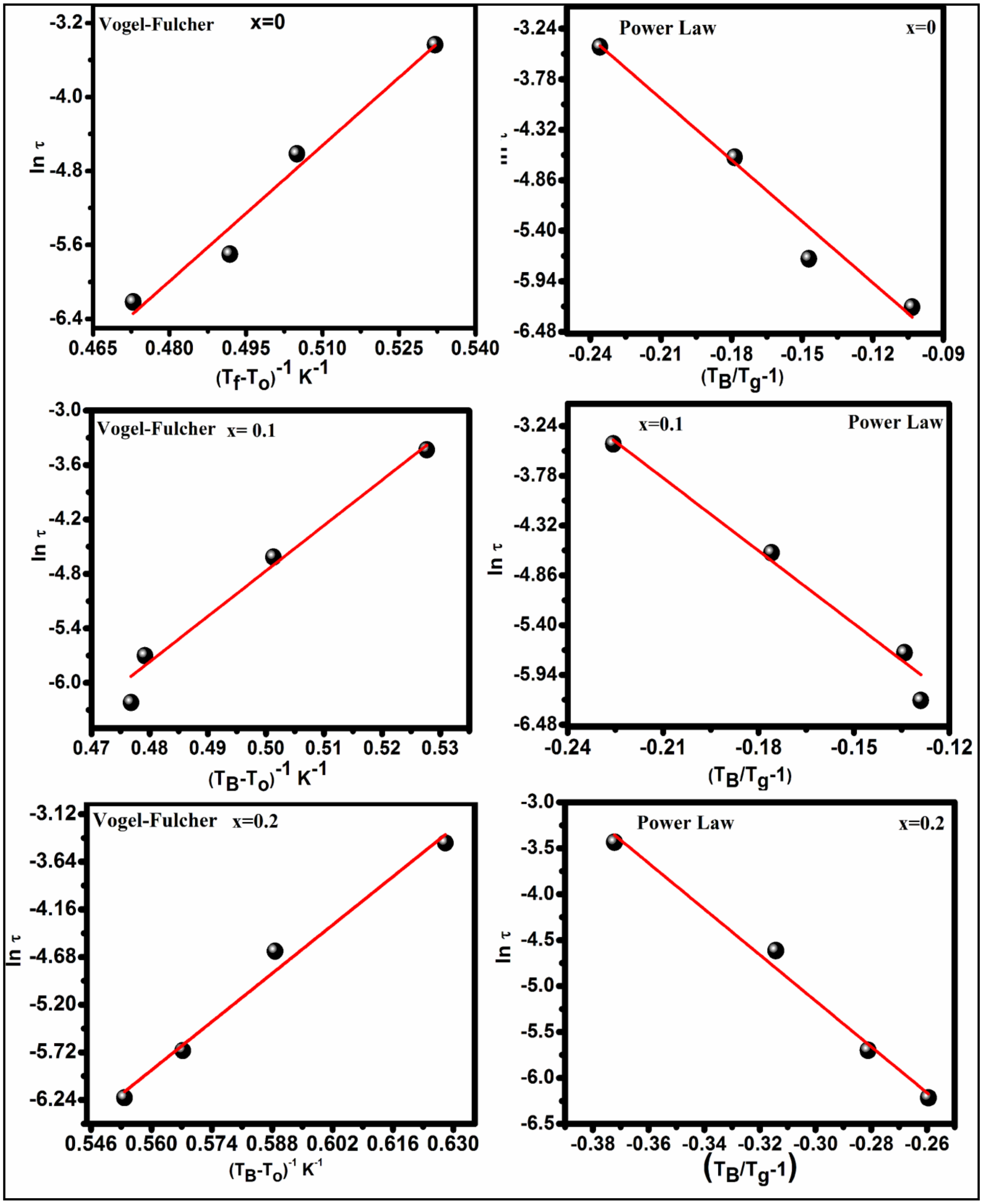

Figure 3.14 *Variation of relaxation time (τ) with T plotted with vogel-fulcher (equation 3.4) and the power law (equation 3.5) for $GdMn_{1-x}Fe_xO_3$ (x= 0, 0.1 and 0.2). The solid line represents the fitting with experimental data point.*

3.4 Conclusions

The effect of Fe doping on the evolution of structure and rich sequence of magnetic transitions in $GdMnO_3$ nanoparticles synthesized through sol-gel technique was studied using XRD, Raman, XPS, magnetization and ac susceptibility measurements. XRD revealed pure phase, an orthorhombic structure with Pbnm space group in $GdMn_{1-x}Fe_xO_3$ (x = 0, 0.1 and 0.2). The Rietveld refinement established the O' type orthorhombic structure with contraction in a and b lattice parameters and expansion in c leading to decrease in lattice volume. The Jahn-Teller (J-T) distortion factor calculated using the bond lengths obtained from Rietveld refinement was found to reduce with an increase in Fe concentration. The lattice contraction was attributed to the presence of Mn^{4+} with oxygen vacancies confirmed through XPS analysis. The observed decrease in J-T distortion resulted from the asymmetric stretching bond located at 487 cm^{-1} in Raman spectra. Magnetic measurements showed that Neel temperature increased from ~42 to ~84 K with an increase in Fe concentration up to 20 at%. The maximum magnetization measured at 70 kOe decreased with increasing Fe concentration whereas the coercivity enhanced by two-fold. The maximum magnetization diminished on account of Mn^{4+} ions, whereas enhancement in H_c was attributed to the increase in bond angle, Mn-O-Mn. The interaction between Mn^{3+} and Mn^{4+} confirmed spin glass and/or cluster glass behavior in $GdMn_{1-x}Fe_xO_3$ perovskites.